\$50 WILLIAMS

Contents lists available at ScienceDirect

### Earth and Planetary Science Letters

www.elsevier.com/locate/epsl



# Inferring crustal viscosity from seismic velocity: Application to the lower crust of Southern California



William J. Shinevar\*, Mark D. Behn, Greg Hirth, Oliver Jagoutz

#### ARTICLE INFO

Article history:
Received 31 January 2018
Received in revised form 9 April 2018
Accepted 27 April 2018
Available online xxxx
Editor: J.P. Avouac

Keywords: lower crust viscosity stress rheology Southern California composition

#### ABSTRACT

We investigate the role of composition on the viscosity of the lower crust through a joint inversion of seismic P-wave  $(V_p)$  and S-wave  $(V_s)$  velocities. We determine the efficacy of using seismic velocity to constrain viscosity, extending previous research demonstrating robust relationships between seismic velocity and crustal composition, as well as crustal composition and viscosity. First, we calculate equilibrium mineral assemblages and seismic velocities for a global compilation of crustal rocks at relevant pressures and temperatures. Second, we use a rheological mixing model that incorporates singlephase flow laws for major crust-forming minerals to calculate aggregate viscosity from predicted mineral assemblages. We find a robust correlation between crustal viscosity and  $V_p$  together with  $V_s$  in the  $\alpha$ -quartz regime. Using seismic data, geodetic surface strain rates, and heat flow measurements from Southern California, our method predicts that lower crustal viscosity varies regionally by four orders of magnitude, and lower crustal stress varies by three orders of magnitude at 25 km depth. At least half of the total variability in stress can be attributed to composition, implying that regional lithology has a significant effect on lower crustal geodynamics. Finally, we use our method to predict the depth of the brittle-ductile transition and compare this to regional variations of the seismic-aseismic transition. The variations in the seismic-aseismic transition are not explained by the variations in our model rheology inferred from the geophysical observations. Thus, we conclude that fabric development, in conjunction with compositional variations (i.e., quartz and mica content), is required to explain the regional changes in the seismic-aseismic transition.

© 2018 Elsevier B.V. All rights reserved.

#### 1. Introduction

The viscosity structure of the lower crust and upper mantle controls deformation processes such as post-seismic creep (e.g., Freed et al., 2007), lower crustal flow (e.g., Clark et al., 2005), post-glacial isostatic rebound (e.g., Jull and McKenzie, 1996), and orogenesis. Estimates of crustal and upper mantle viscosity are typically constrained by analyses of post-seismic relaxation, paleolake shoreline deflection, global flow and stress models, and laboratory derived flow laws for crust-forming rocks and minerals (e.g., Thatcher and Pollitz, 2008; England et al., 2013; Shi et al., 2015; Humphreys and Coblentz, 2007; Bürgmann and Dresen, 2008). In most previous studies based on laboratory data the rheology of the lower continental crust was approximated using a flow law for a dominant mineral phase (e.g., quartz or feldspar). However, the lower crust is composed of multiple mineral phases with variable strength and abundances that are controlled by the bulk composition, pressure, and temperature conditions. Thus, to accurately

E-mail address: shinevar@mit.edu (W.J. Shinevar).

calculate crustal viscosity, composition, pressure, and temperature must be constrained.

Seismic P-wave  $(V_p)$  and S-wave  $(V_s)$  velocities are frequently used as a proxy for crustal composition. Christensen and Mooney (1995) measured  $V_p$  for a variety of igneous and metamorphic rocks and compared the measurements to average continental crustal seismic profiles. With knowledge of field geology, they created a petrological model of the continental crust. Rudnick and Fountain (1995) estimated average mid and lower crustal compositions by comparing the predicted  $V_p$  of granulites to  $V_p$  profiles constructed for typical tectonic environments. Christensen (1996) added  $V_s$  to the analysis of crustal composition and showed that crustal  $V_p/V_s$  ratios are nominally independent of temperature, but sensitive to quartz abundance, with a strong linear correlation between  $V_p/V_s$  and silica content (between 55 and 75 wt% SiO<sub>2</sub>). More recently, Shillington et al. (2013) and Jagoutz and Behn (2013) combined thermodynamic modeling,  $V_p/V_s$ , and  $V_p$ to constrain the composition of arc lower crust, showing that the additional information provided by  $V_p/V_s$  gives a much tighter constraint on composition than is obtained by  $V_s$  alone. Other studies have linked seismic data to the mechanical properties of the crust. For example, Lowry and Pérez-Gussinyé (2011) found

<sup>\*</sup> Corresponding author.

a relationship between  $V_p/V_s$  and effective elastic thickness in the western United States, pointing toward a relationship between seismic velocity and viscosity.

Here, we investigate the relationship between aggregate viscosity and seismic velocities by calculating a fit between viscosity (estimated using multi-phase rheological mixing theory) and seismic P-wave and S-wave velocity for a wide range of crustal compositions at typical crustal pressures and temperatures. Our analyses show that while neither  $V_p$  nor  $V_s$  alone robustly predict aggregate viscosity, together  $V_p$  and  $V_s$  predict aggregate viscosity within a factor of 2 at most crustal conditions. We apply our method to calculate the viscosity of the lower crust in Southern California, taking advantage of data from a densely instrumented region. We discuss the benefits and limitations of our methodology in the context of constraining compositional controls on upper and lower crustal viscosity – and compare the predicted depth to the brittle–ductile transition with observed seismic–aseismic transitions.

#### 2. Methods

To estimate aggregate crustal viscosity from  $V_p$  and  $V_s$  data, we use the following 4-step approach: 1) create a rock database that spans crustal composition space; 2) calculate equilibrium mineral assemblages and seismic velocities for each composition in the rock database over a range of relevant pressure (P) and temperature (T); 3) calculate the aggregate viscosity for each composition at all P-T conditions; and 4) compile our estimates of  $V_p$ ,  $V_s$ , and aggregate viscosity over crustal P-T space to derive a generic relationship between viscosity and P, T,  $V_p$ ,  $V_s$ , and stress or strain rate. Finally, because viscosity is strongly sensitive to temperature, one must incorporate additional constraints when applying our methodology to specific geologic settings. Below, we describe each of these steps as well as our methodology for constraining crustal temperatures in Southern California.

#### 2.1. Compositional database for crustal rocks

To create a compositional database for crustal rocks, we take all available whole rock compositions for the continental US and Alaska from Earthchem (www.earthchem.org). We filter out carbonates (>2 wt% CO<sub>2</sub>) and samples with oxide analyses that sum to less than 95 wt% or more than 102 wt%. To this dataset, we add arc rocks from the compilation of Kelemen and Behn (2016), which includes Archean and post-Archean massif data from Hacker et al. (2015), crustal xenolith and amphibolite data from Huang et al. (2013), and lavas and plutonic rocks from the Aleutians, Izu-Bonin-Marianas, Kohistan (Jagoutz and Schmidt, 2012) and Talkeetna (Kelemen et al., 2014) arcs. The final crustal database includes 96,388 samples. To facilitate the thermodynamic calculations presented below, we sub-sampled this database by first sorting the compositions by wt% SiO2 and then taking every 28th sample, creating a representative database of 3442 samples. Subsampling does not alter the frequency distribution for any of the major oxides (Supplemental Fig. 1); a principal component analysis of the total and sub-sampled data sets produces similar sub-spaces (Supplemental Tables 1 and 2). Thus, the relationships derived from the sub-sampled data accurately reflect those present in the total composition space.

## 2.2. Calculation of equilibrium mineral assemblages and seismic velocity

To calculate the equilibrium mineral assemblage for each composition, we use the Gibbs free energy minimization routine Perple\_X (Connolly, 2009). We calculate mineral assemblages over

crustal temperatures  $(300-1000\,^{\circ}\text{C})$  and pressures  $(0.1-1.2\,\text{GPa})$ . We assume a minimum equilibrium temperature of  $500\,^{\circ}\text{C}$ , a reasonable lower bound for net transfer reactions under hydrous crustal conditions (Austrheim, 1998). The lower continental crust typically contains  $0-1\,\text{wt}\%\,\text{H}_2\text{O}$  (Huang et al., 2013). In this study, we only consider anhydrous mineral assemblages and incorporate the influence of  $\text{H}_2\text{O}$  through its effect on the viscosity of nominally anhydrous mineral phases (see below). The role of hydrous phases (e.g., amphibole and mica) is ignored in our calculations due to the complexities of quantitatively incorporating their effects on rheology (Shinevar et al., 2015); however, we discuss their potential role on crustal viscosity in the Section 4.

For all Perple\_X calculations, we assume that 25 mol% of the total iron oxide is ferric (Cottrell and Kelley, 2011; Kelley and Cottrell, 2012); variations in this value have little influence on aggregate viscosity and seismic wave speeds. Solution models for crustal minerals are taken from Hacker (2008). Seismic velocities are calculated using a compilation of mineral properties (Abers and Hacker, 2016) implemented into Perple\_X with the  $\alpha$ - $\beta$  quartz implementation used by Jagoutz and Behn (2013).

#### 2.3. Calculation of aggregate viscosity

To calculate crustal viscosity at a given condition, we employ mixing theory to determine the aggregate viscosity for each equilibrium mineral assemblage. We only consider deformation via wet dislocation creep. This assumes that diffusion creep is not an important mechanism controlling the rheology of the lower crust (see Section 4 for further discussion). Theoretical and experimental investigations show a power law relation between stress  $(\sigma)$  and strain rate  $(\dot{\epsilon})$  with the form:

$$\dot{\epsilon} = A f_{\rm H_2O}^r \sigma^n \exp\left(\frac{-(E + PV)}{RT}\right),\tag{1}$$

where A is the pre-exponential factor,  $f_{\rm H_2O}$  is water fugacity, r is the fugacity exponent, n is the stress exponent, E is the activation energy, V is the activation volume, and R is the gas constant. To estimate water fugacity, we use an exponential fit to water fugacity values along crustal geotherms (Shinevar et al., 2015):

$$f_{\rm H_2O} = a_{\rm H_2O} B_1 \exp\left(-\frac{B_2 + P B_3}{RT}\right) \tag{2}$$

where  $a_{\rm H_2O}$  is the water activity and  $B_1$ ,  $B_2$ , and  $B_3$  are empirically fit constants. We explore fugacity values using water activities between 0.01 and 1. Aggregate viscosities are calculated for strain rates ranging from  $10^{-12}$  to  $10^{-16}$  s<sup>-1</sup> and shear stresses ranging from 1 to 100 MPa.

The effective viscosity of major crust-forming minerals varies by almost 3.5 orders of magnitude at 650 °C - between the strongest minerals (olivine and pyroxene) and the weakest anhydrous mineral (quartz) (Fig. 1). Here we consider five major crust-forming minerals: quartz, feldspar (plagioclase + alkali feldspar), pyroxene (orthopyroxene + clinopyroxene), garnet, and olivine. Wet dislocation creep flow laws for quartz, feldspar, pyroxene, and olivine are taken from Hirth et al. (2001), Rybacki et al. (2006), Dimanov and Dresen (2005), and Hirth and Kohlsedt (2003), respectively. The pyroxene flow law was modified by introducing a linear water fugacity term, in which the published pre-exponential coefficient is recalculated accordingly ( $A = A_{experimental}/fH_2O$  for the experimental fugacity). The pre-exponential coefficients are corrected to express the relationship between the second invariants of stress and strain rate rather than uniaxial or simple shear. All garnet flow laws (e.g. Karato et al., 1995; Xu et al., 2013) found in the literature predict effective viscosities lower than plagioclase at lower crustal

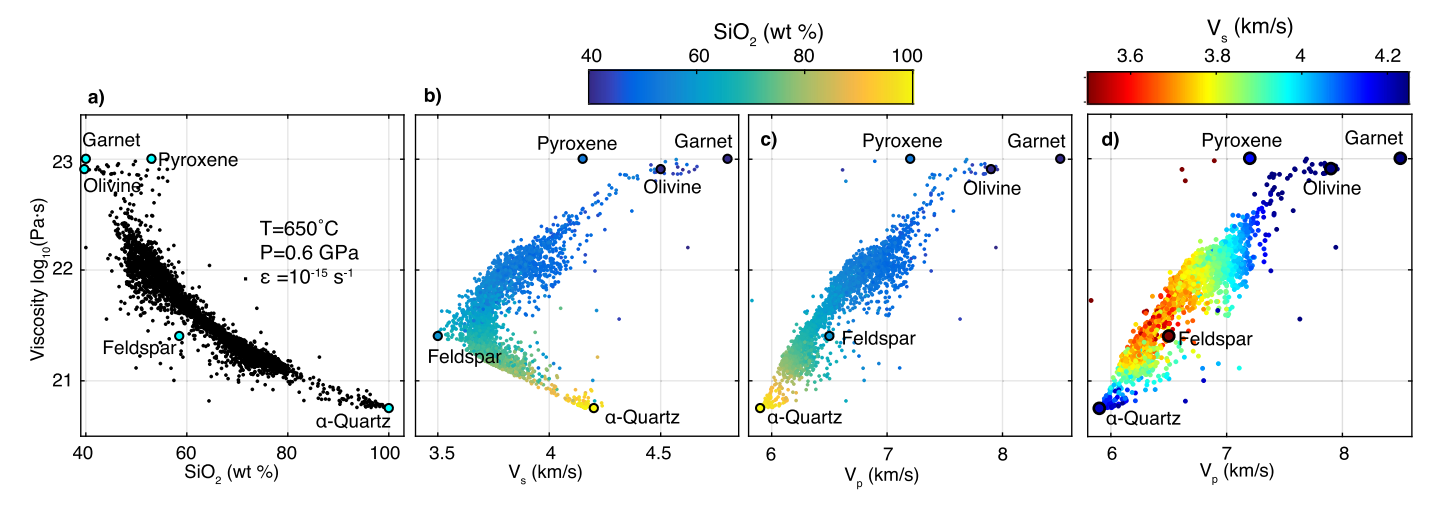


Fig. 1. a) Calculated aggregate viscosity as a function of SiO<sub>2</sub> for the total rock database at T = 650 °C, P = 0.6 GPa,  $\dot{\epsilon} = 10^{-15} \text{ s}^{-1}$ ,  $a_{\text{H}_2\text{O}} = 1.0$ . b + c) Viscosity as a function of  $V_s$  (left) and  $V_p$  (right) colored by wt% SiO<sub>2</sub>. d) Viscosity as a function of  $V_p$  colored by  $V_s$ . See Section 2 for explanations of total rock database, velocity calculations, and viscosity calculations. (For interpretation of the colors in the figure(s), the reader is referred to the web version of this article.)

conditions (see Supplementary Fig. S2 of Shinevar et al., 2015), but abundant field evidence suggests that garnet is stronger than plagioclase at crustal conditions (e.g., Ji and Martignole, 1994). Thus, we assume that garnet has the same viscosity as pyroxene, which is 1-2 orders of magnitude greater than plagioclase at crustal con-

For many bulk compositions, phase equilibrium calculations predict additional mineral phases; we only calculate viscosity for samples comprised of >90 vol% quartz, feldspar, pyroxene, garnet and olivine. This condition is met for >95% of the compositions in our representative database at every P-T condition; only these samples are included in our inversion described below. We assume that remaining secondary phases (<10 vol%) have a negligible effect on the bulk viscosity (see Section 4 for further discussion on the role of hydrous phases).

We use the mixing model of Huet et al. (2014) to estimate aggregate viscosity from the calculated mineral modes. This mixing model is based on the minimization of power dissipation during deformation. Huet et al. (2014) define the effective aggregate vis-

$$\eta_{aggregate} = \sum_{i} \frac{\phi_{i} n_{i}}{n_{i} + 1} \prod_{i} \left( \eta_{i} \frac{n_{i} + 1}{n_{i}} \right)^{\sum_{i} \phi_{j} \alpha_{j} n_{j}}$$
(3)

where  $\phi_i$  and  $n_i$  are the volume percentage and stress exponent of phase i, respectively, and the parameter  $\alpha$  is defined for each phase as  $\alpha_i = \prod_{i \neq j} (n_j + 1)$ . This method assumes that the rock is homogeneous and isotropic. As noted above we use single-phase flow law parameters for wet dislocation creep for all phases. Fig. 1a shows the strong dependence of aggregate viscosity on composition (as reflected by silica content) using Eq. (3).

#### 2.4. Local inversion of viscosity from seismic velocity

We invert for a relationship between viscosity and  $V_p$  and  $V_s$ using all compositions at each individual P, T, strain rate and water activity. The goal of this exercise is to deduce where in crustal parameter space a robust relationship exists between viscosity and seismic velocity. For instance, Fig. 1 shows relationships between SiO<sub>2</sub>,  $V_p$ ,  $V_s$ , and aggregate viscosity at hot lower crustal condition (0.6 GPa, 650 °C,  $10^{-15}$  s<sup>-1</sup>,  $a_{\rm H_2O}=1$ ).  $V_s$  (which can be constrained regionally from ambient noise tomography and surface wave studies) provides a poor fit to aggregate viscosity (Fig. 1b). By contrast,  $V_p$  (which is typically obtained from body waves, active source studies, or assumptions regarding Poisson's ratio) constrains aggregate viscosity to one order of magnitude (Fig. 1c). Combining  $V_p$  and  $V_s$  improves this fit to less than half an order of magnitude

The relationship between aggregate viscosity and seismic velocity is based on the functional form of the flow laws. By definition. viscosity  $(\eta)$  is defined as the ratio of stress to strain rate. Using Eq. (1), we formulate viscosity as a function of strain rate  $(\eta_{\dot{\epsilon}})$  or stress  $(\eta_{\sigma})$ :

$$\eta_{\dot{\epsilon}} = \dot{\epsilon}^{\frac{1}{n} - 1} f_{\text{H}_2\text{O}}^{-\frac{r}{n}} A^{\frac{-1}{n}} \exp\left(\frac{(E + PV)}{nRT}\right)$$
(4a)

$$\eta_{\sigma} = \sigma^{1-n} f_{H_2O}^{-r} A^{-1} \exp\left(\frac{(E+PV)}{RT}\right).$$
(4b)

Taking the logarithm of Eqs. (4a) and (4b) gives:

$$\log(\eta_{\dot{\epsilon}}) = \left(\frac{1}{n} - 1\right) \log(\dot{\epsilon}) - \frac{r}{n} \log(f_{\text{H}_2\text{O}})$$

$$-\frac{1}{n} \log(A) + \frac{E + PV}{nRT}$$

$$\log(\eta_{\sigma}) = (1 - n) \log(\sigma) - r \log(f_{\text{H}_2\text{O}})$$
(5a)

$$-\log(A) + \frac{E + PV}{RT}. (5b)$$

Because the stress exponent n and fugacity exponent r are similar between flow laws at a given set of  $P-T-\dot{\epsilon}-f_{\rm H_2O}$  or  $P-T-\sigma-f_{\rm H_2O}$ conditions, we assume the first two terms are constant. The latter two terms (which include the pre-exponential factor, activation energy, and activation volume) are approximated as linear combinations of  $V_p$  and  $V_s$ . With these assumptions, the relationship between viscosity and  $V_p$  and  $V_s$  becomes:

$$\log(\eta) = a + bV_p + cV_s \tag{6}$$

where a, b, and c are constants. Using the calculated aggregate viscosities and seismic velocities for each composition, we calculate a least squares fit to determine the values of a, b, and c at each  $P-T-\dot{\epsilon}-f_{\rm H_2O}$  or  $P-T-\sigma-f_{\rm H_2O}$  condition. We refer to these fits as "local inversions" because the parameters are only fit at a single condition.

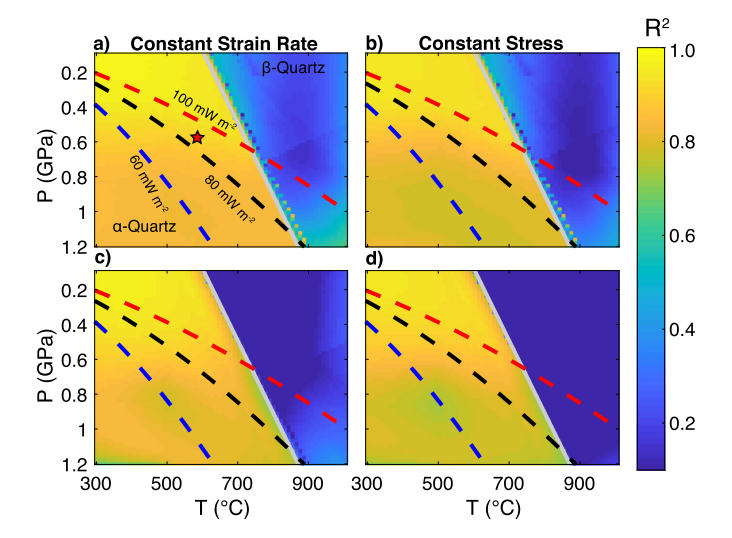


**Fig. 2. a** and **b**) Each point in these figures denotes  $R^2$  (goodness of fit) for fits at a constant P-T (Eq. (6)) and either constant strain rate (left) or stress (right) ( $\dot{\epsilon}=10^{-15}~{\rm s}^{-1}$  or  $\sigma=10$  MPa,  $a_{\rm H_2O}=1.0$ ). Grey line denotes the  $\alpha$ - $\beta$  quartz transition. 60 (blue,  $\sim15~{\rm ^{\circ}C/km^{-1}}$ ), 80 (black,  $\sim20~{\rm ^{\circ}C/km^{-1}}$ ), and 100 (red,  $\sim26~{\rm ^{\circ}C\,km^{-1}}$ ) mW m $^{-2}$  geotherms shown for reference. Red star denotes the conditions in Fig. 1. **c** and **d**) Each point in these figures denotes the R $^2$  for the generic fit at that P-T condition (Eq. (7a) and (7b) respectively) using all the data from the  $\alpha$  quartz regime.

Figs. 2a and b show the R<sup>2</sup> values for the local strain rate and stress inversions over a range of P-T conditions. Fits for the parameters in Eq. (6) provide a good estimate of viscosity for both constant strain rate and stress ( $R^2 > 0.8$ ) in the  $\alpha$ -quartz regime, but a poor fit in the  $\beta$ -quartz regime. For reference, the  $\alpha$ - $\beta$  quartz transition occurs around 750 °C at 25 km depth (Fig. 2). The inversion fits well and produces residuals that form a Gaussian distribution around  $0\log_{10}$  (Pas) in the  $\alpha$ -quartz regime because quartz. feldspar, and the mafic minerals (olivine, pyroxene, and garnet) form three distinct regions in velocity-viscosity space (Fig. 1). In the  $\beta$ -quartz regime, the inversion fails due to the sharp increase in the bulk modulus of quartz-bearing rocks, resulting in a  $V_p$ comparable to mafic compositions (Supplemental Fig. 2). Because  $\alpha$ - and  $\beta$ -quartz have similar effective viscosities, the mapping from velocity to viscosity becomes multivalued in the  $\beta$ -quartz field, producing poor fits (Fig. 2).

To create a generic inversion for viscosity that is valid across crustal conditions, we parameterize the constants a, b, and c in Eq. (6) as a function  $P-T-\dot{\epsilon}-f_{\rm H_2O}$  or  $P-T-\sigma-f_{\rm H_2O}$ . The log strain rate and log stress dependence of log viscosity is linear (Eq. 5a and 5b). Inputting fugacity from Eq. (2) into Eq. (5) and using logarithm identities, it can be shown that the log water activity dependence of the log viscosity is also linear. Based on the general expectation that rheological properties scale with the elastic properties (Karato, 2012), we parameterize  $\log(A)$ , E, and V as linear combinations of

 $V_p$  and  $V_s$  (similar to Eq. (6)). This results in the following equations for constant strain rate and stress:

$$\begin{split} \log_{10}(\eta_{\dot{\epsilon}}) \\ &= a_1 + a_2 \log_{10} \dot{\epsilon} + a_3 \log_{10} a_{\text{H}_2\text{O}} + \frac{1000 a_4}{T} + \frac{1000 a_5 P}{T} \\ &+ b_1 V_p + \frac{1000 b_2 V_p}{T} + \frac{1000 b_3 P V_p}{T} \\ &+ c_1 V_s + \frac{1000 c_2 V_s}{T} + \frac{1000 c_3 P V_s}{T} \end{split} \tag{7a}$$

$$\log_{10}(\eta_{\sigma})$$

$$&= a_1 + a_2 \log_{10} \sigma + a_3 \log_{10} a_{\text{H}_2\text{O}} + \frac{1000 a_4}{T} + \frac{1000 a_5 P}{T} \\ &+ b_1 V_p + \frac{1000 b_2 V_p}{T} + \frac{1000 b_3 P V_p}{T} \\ &+ c_1 V_s + \frac{1000 c_2 V_s}{T} + \frac{1000 c_3 P V_s}{T} \end{aligned} \tag{7b}$$

with  $\eta$  in Pa s, T in K, P in Pa,  $V_p$  and  $V_s$  in km s<sup>-1</sup>,  $\sigma$  in Pa, and  $\dot{\epsilon}$  in s<sup>-1</sup>. Using all of the calculated velocity and viscosity data in the  $\alpha$ -quartz field, we invert for the parameters in Equations (7a) and (7b) (Table 1). Equation (7a) fits the data with a RMSE of 0.18 log<sub>10</sub> (Pa s) and a R<sup>2</sup> of 0.96; Equation (7b) fits the data with an RMSE of 0.86 log<sub>10</sub> (Pa s) and a R<sup>2</sup> of 0.94. The error is larger for the constant stress fit because the viscosities at constant stress vary more than for constant strain rate. These fits produce Gaussian residuals (Supplemental Figs. 3 and 4).

The error in the generic aggregate viscosity-velocity inversion is approximately the same as the average error calculated over the  $\alpha$ -quartz regime from the local inversions at each P-T condition (compare Figs. 2c and 2d to Figs. 2a and 2b). Moreover, the resulting generic inversion for aggregate viscosity agrees with intuition; aggregate viscosity decreases with increasing temperature, strain rate and water activity, but increases with increasing pressure. Further, aggregate viscosity increases with increasing  $V_p$ , and for most conditions, decreases with increasing  $V_s$ . Aggregate viscosity also scales positively with  $V_p/V_s$  at a given set of P-T conditions; however, the best fits are found by including independent estimates of  $V_p$  and  $V_s$ .

We have investigated the sensitivity of our approach at conditions appropriate for the lower crust. For a  $V_p$  of 7.0 km s<sup>-1</sup> and a  $V_s$  of 4.0 km s<sup>-1</sup> at 0.8 GPa, a change in temperature from 650 °C to 750 °C decreases the aggregate viscosity by a factor of 3.9. For comparison, a change in  $V_p$  or  $V_s$  by 0.2 km s<sup>-1</sup> at the same P-T conditions promotes a change in viscosity by a factor of 1.5 or 1.4, respectively. A factor of 10 increase in strain-rate produces a factor of 5 decrease in strain rate. A factor of 10 decrease in water activity results in a factor of 1.9 increase in viscosity.

**Table 1** Parameter values for Eq. (7a) and (7b).

Parameter (units)	Constant strain rate (Eq. (7a))	Constant stress (Eq. (7b))
a <sub>1</sub> (log <sub>10</sub> (Pas))	-0.3780	7.4290
$a_2 (\log_{10} (Pas) \log_{10}(s))$	-0.7123	-2.4975
$a_3 (\log_{10} (Pas))$	-0.2877	-1.0000
$a_4 (\log_{10} (Pas)K)$	5.2041	-9.2960
$a_5 (\log_{10} (Pas) K G Pa^{-1})$	2.7066	11.9028
$b_1 (\log_{10} (\text{Pa s}) \text{ s km}^{-1})$	-2.3587	-8.4493
$b_2 (\log_{10} (\text{Pa s}) \text{ s K km}^{-1})$	3.1622	11.7487
$b_3 (\log_{10} (\text{Pa s}) \text{ s K km}^{-1} \text{ Pa}^{-1})$	0.0455*1e-9	-0.2711*1e-9
$c_1 (\log_{10} (\text{Pa s}) \text{ s km}^{-1})$	5.5208	13.7598
$c_2 (\log_{10} (\text{Pa s}) \text{ s K km}^{-1})$	-5.3804	-13.0257
$c_3 (\log_{10} (\text{Pa s}) \text{ s K km}^{-1} \text{ Pa}^{-1})$	-0.8413*1e-9	-2.9594*1e-9

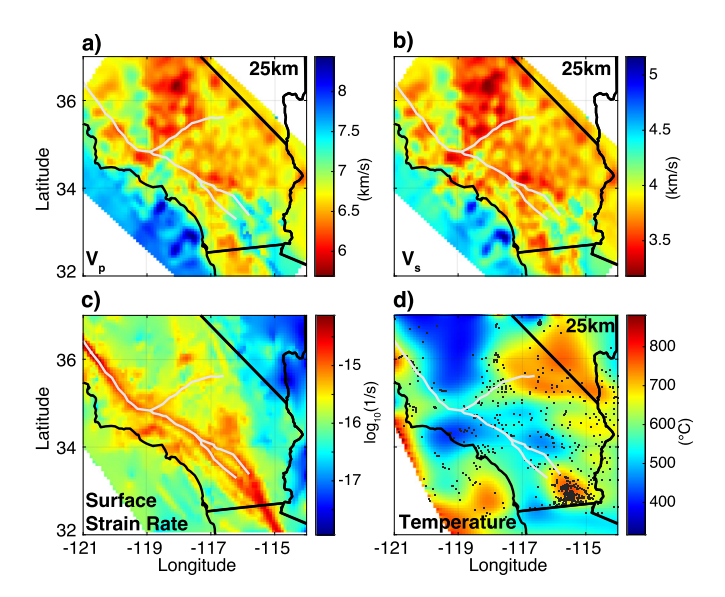


**Fig. 3. a + b)**  $V_p$  (left),  $V_s$  (right) at 25 km depth from the Community Velocity Model-S4.26 (Lee et al., 2014). White regions indicate areas outside of model domain or with predicted mantle velocities. **c)** Second invariant of surface strain rate (Kraner et al., 2018). **d)** Modeled temperature of Southern California at 25 km depth (see Section 2 for discussion). Grey lines indicate the San Andreas, Garlock, and San lacinto Faults.

#### 2.5. California input data and geotherm calculations

To use Eq. (7a) to investigate the viscosity structure of Southern California, we need seismic velocity data as well as the  $P-T-\dot{\epsilon}-a_{H_2O}$ conditions in the crust. Our inversion method requires independently calculated P and S-wave velocities. Assuming a constant  $V_n/V_s$  ratio negates the compositional effects that our method aims to quantify as shown in Fig. 1. For seismic data, we use the Community Velocity Model-S4.26 (Lee et al., 2014), which provides independent constraints on  $V_p$  and  $V_s$  (Fig. 3a and b). In some regions the velocities predicted by the Community Velocity Model (CVM), are not consistent with the velocities calculated from any of the compositions in our database. We do not plot viscosities in our figures when the CVM velocity is more than 0.1 km s<sup>-1</sup> different than the  $V_p$  and  $V_s$  calculated for all of the samples in our database at the inferred P-T conditions. Many of the areas with the largest error are mountainous (Sierra Nevadas and Transverse Ranges), suggesting errors due to topographic effects not accounted for in the CVM (Lee et al., 2014). Velocity errors are shown for 25 km depth in Supplemental Fig. 5 and along a cross section across the Mojave in Supplemental Fig. 6.

To account for the wide variation in deformation rates across Southern California, we approximate strain rate in the lower crust with the second invariant of surface strain rate from Kraner et al. (2018) (Fig. 3c). We acknowledge the uncertainties in applying surface strain rates to the viscously deforming lower crust (e.g. interseismic elastic strain buildup at the surface and strain localization in the viscous regime), however it is a good starting point for accounting for regional variations in strain rate. To estimate pressure at depth, we use an average continental crustal density of 2800  $kg m^{-3}$ . We use a water activity of 1. To estimate temperature within the crust, we rely on heat flow measurements from Williams and DeAngelo (2011) and the SMU Geothermal Database (http://geothermal.smu.edu/gtda/). We first use a natural neighbor scheme to interpolate the heat flow data to the same grid as the seismic velocity model. We then calculate temperature as a function of depth at each grid point assuming a steady-state 1-D geotherm following the assumption that the heat production in the

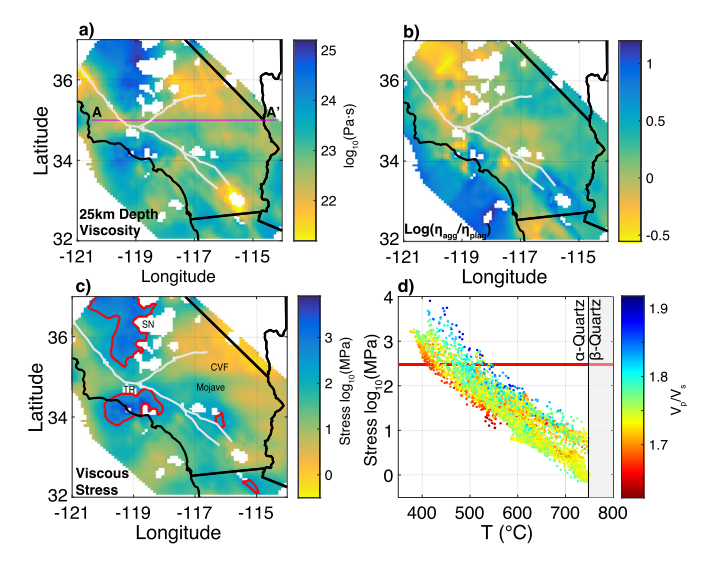


**Fig. 4. a**) Viscosities calculated for Southern California at 25 km depth using Eq. (7a) using data shown in Fig. 3 assuming  $a_{\rm H_2O}=1.0$ . **b**)  $\log_{10}\frac{\eta_{\rm aggregate}}{\eta_{\rm plugloclaise}}$  the same depth (see Section 3 for explanation). **c**) Ductile stress field at the same depth. Red lines contour areas where the predicted ductile stress is greater than the yield stress. White regions denote regions lacking data, regions predicted to be in the β quartz regime (T > 750 °C at 25 km depth), or regions where the seismic velocities are greater than error away from predicted possible velocities used to fit the model. Grey lines indicate the San Andreas, Garlock, and San Jacinto Faults. Pink line denotes location for Fig. 5. CVF = Cima Volcanic Field, SN: Sierra Nevadas, TR: Transverse Ranges **d**) Stress from **c**) scattered against the temperature field (Fig. 3d) colored by  $V_D/V_S$ . Red line depicts the yield stress.

upper crust accounts for 40% of the measured surface heat flow (Pollack and Chapman, 1977). We assume a constant heat production in the upper crust (<15 km depth). Varying the distribution of heat flow in the upper crust does not have a large impact on our estimate of lower crustal temperatures. We assume a constant lower crust heat production of 0.5  $\mu$ W m<sup>-3</sup> based on average values for exposed lower crustal rocks in the Sierra Nevadas (Brady et al., 2006). Thermal conductivity is taken to be a function of temperature (Durham et al., 1987):

$$k(T) = 2.264 - \frac{618.2}{T} + 3.0 \left( \frac{355.6}{T} - 0.3205 \right)$$
 (8)

where k is thermal conductivity in W m<sup>-1</sup> K<sup>-1</sup> and T is temperature in K. At 20 °C, the thermal conductivity is 3.0 W m<sup>-1</sup> K<sup>-1</sup>. To remove unrealistic horizontal temperature gradients, we diffuse the temperature field horizontally for five million years assuming constant boundary temperature and a thermal diffusivity of  $10^{-6}$  m<sup>2</sup> s<sup>-1</sup>. Fig. 3d shows the resulting temperature field at 25 km depth, which predict geothermal gradients ranging from 15-35 °C km<sup>-1</sup>. Sources of error in our geotherm calculation include: (1) error in the heat flow measurements; (2) regions where the geotherm is not in steady state (e.g., due to rifting in the Salton Trough, active delamination in the southern Sierra Nevadas (Zandt et al., 2004), or fluid transport); and (3) regions where heat production does not follow our scaling assumption.

#### 3. Application to Southern California

The prolonged tectonic evolution of the plate boundary between the Pacific/Farallon and North American plates has produced a heterogeneous lower crust throughout Southern California. This compositional variability, combined with the availability of high-resolution seismic and heat flow data, make Southern California an excellent testing ground for our methodology. In addition, there is

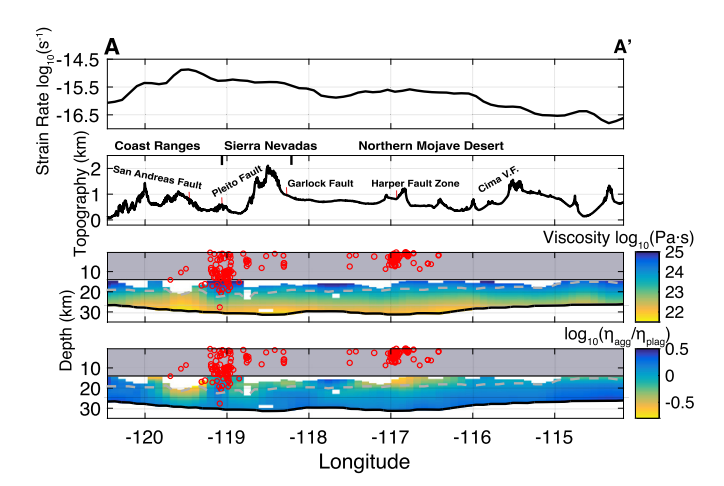


**Fig. 5.** Strain rate, topography, predicted viscosity, and  $\log_{10} \frac{\eta_{\rm oggredue}}{\eta_{\rm plagioclase}}$  (see Section 3 for explanation) along the Mojave at 35°N (A–A′ in Fig. 4). Black lines denote the Moho. Grey dashed line indicates predicted brittle–ductile transition. Red dots indicate earthquake epicenters within 10 km north or south of the cross section. White regions denote regions lacking data, regions predicted to be in the  $\beta$  quartz regime, or regions where the seismic velocities are greater than error away from predicted possible velocities used to fit the model. Grey box denotes upper crust where velocity calculations have misfit with predicted possible velocities, most likely due to porosity effects.

a wide array of geologic, geochemical, and geophysical data available on the California lower crust with which to compare the predicted viscosity structure.

Using Eq. (7a) with our predicted temperatures, surface strain rates, and velocities from the CVM, we calculate aggregate viscosities ranging from  $10^{21}$ – $10^{25}$  Pa s at 25 km depth (Fig. 4a). To highlight compositional variations, we plot  $\log_{10} \frac{\eta_{aggregate}}{\eta_{plagioclase}}$  where  $\eta_{plagioclase}$  is the viscosity calculated by the wet plagioclase flow law at the same conditions (Fig. 4b). Because quartz is the only phase we consider that is weaker than plagioclase,  $\log_{10} \frac{\eta_{aggregate}}{\eta_{plagioclase}} < 0$  (yellow) indicate a rheologically significant fraction of quartz;  $\log_{10} \frac{\eta_{aggregate}}{\eta_{plagioclase}} > 0$  (blue) indicate a rheologically significant fraction of mafic minerals. Our method suggests that the Sierra Nevada and the Salton Trough are comprised of more felsic and more mafic lithologies, respectively. These results agree with the inferred presence of a 30–35 km thick granitic batholith beneath the Sierra Nevada (Ducea and Saleeby, 1998) and evidence for large mafic additions to the lower crust of the Salton Trough (Lachenbruch et al., 1985).

Further, using the input surface strain rate (Kraner et al., 2018) and the aggregate viscosity, we calculate the viscous stress field at 25 km depth. The viscous stress varies between 0.7 MPa and 7 GPa (Fig. 4c). To illustrate regions predicted to be in the brittle regime at 25 km depth, we compare the viscous stress to the frictional stress calculated assuming strike-slip conditions with a hydrostatic pore-fluid pressure (Zoback and Townsend, 2001, Eq. (7b)) and a friction coefficient of 0.6. The high viscous stresses in the two coldest regions (the Transverse Ranges and the Western Sierra Nevadas) clearly exceed the brittle strength (contoured by red lines in Fig. 4c), in agreement with the presence of earthquakes below 25 km in the Transverse Ranges. The viscous stress is relatively continuous with the largest gradients coinciding with the largest temperature gradients. Plotting stress from Fig. 4c against temperature from Fig. 3d, indicates a one and a half order of magnitude variation in stress at a given temperature due to compositional and strain rate effects (Fig. 4d).

A cross section of the predicted viscosities across the northern Mojave (Fig. 5) indicates both vertical and horizontal variations in composition in Southern California (as depicted by the change in

 $\log_{10} \frac{\eta_{aggregate}}{\eta_{plagioclase}}$ ). The crust becomes more mafic towards the east in the Mojave (i.e.,  $\log_{10} \frac{\eta_{aggregate}}{\eta_{plagioclase}}$  increases) and is most felsic (i.e., lowest  $\log_{10} \frac{\eta_{aggregate}}{\eta_{plagioclase}}$ ) under the Sierra Nevadas and Coast Ranges. In general, the upper crust has an aggregate viscosity less than plagioclase;  $\log_{10} \frac{\eta_{aggregate}}{\eta_{plagioclase}}$  increases with depth in accord with the abundance of mafic lower crustal xenoliths from the Cima volcanic field (Hanchar et al., 1994). The crustal aggregate viscosities also agree well with independent analyses of post-seismic creep ( $\eta > 10^{21}$  Pa s) in the Mojave Desert (Freed and Bürgmann, 2004; Freed et al., 2007).

To isolate the role of composition, we normalize the aggregate viscosity at a depth of 25 km (Fig. 4a) to two constant strain rates and compare it to single-phase flow laws for major crust forming minerals (Fig. 6). The normalized aggregate viscosities at 25 km depth vary by almost four orders of magnitude over a temperature range of approximately 400 °C (Fig. 6). Overall, plagioclase provides the best approximation to the aggregate viscosities. However, at any given temperature, the variation due to composition ranges up to one and a half orders of magnitude. Thus, although the plagioclase flow law captures the general variability of viscosity with temperature, the role of composition should be considered in geodynamic models of compositionally heterogeneous regions like Southern California.

Finally, the temperature dependence of the aggregate viscosities is slightly less than plagioclase – implying that the bulk behavior of the crust can be characterized by a lower activation enthalpy over stress exponent ratio (E/n). Fitting an Arrhenius relation to the aggregate viscosities at 25 km depth using a stress exponent of 3.5 (derived from Eq. (7a)), the aggregate flow law  $(R^2$  of 0.91 and RMSE of  $0.25 \log_{10} (Pas)$ ) for Southern California is

$$\dot{\epsilon} = A f_{\rm H_2O}^1 \sigma^{3.5} \exp\left(\frac{-E}{RT}\right),\tag{9}$$

where  $E = 340 \pm 20$  kJ mol<sup>-1</sup> and  $\log_{10}(A) = -23.9 \pm 0.2 \log_{10}(Pa^{-3.5} s^{-1})$  (black line in Fig. 6). This aggregate flow law has an E/n ratio of 96 kJ mol<sup>-1</sup>; the plagioclase flow law has E/n = 115 kJ mol<sup>-1</sup> (Dimanov and Dresen, 2005).

#### 4. Discussion

In this section, we discuss the implications and limitations of our methodology. First, we discuss weakening mechanisms that are not included and their potential effects on crustal viscosity in Southern California. Second, we compare the depth of the brittle-ductile transition predicted by our method to the seismic–aseismic transition and discuss implications for the compositional effects on crustal strength profiles.

#### 4.1. Weakening mechanisms

Our methodology calculates aggregate viscosity assuming isotropic material properties. In addition, we do not consider the effects of hydrous phases, melt, grain size reduction/diffusion creep, and/or strain localization and fabric formation in shear zones. Below we describe the effects of each of these weakening mechanisms on our predicted viscosity.

The presence of water in the lower crust stabilizes hydrous minerals such as amphibole and mica. While the flow laws for these minerals are poorly constrained, some information on their strength is available. Amphibole is relatively strong, with a viscosity comparable to that of pyroxene (Hacker and Christie, 1990). Thus, the addition of amphibole is unlikely to dramatically alter the viscosity of mafic rocks from our estimates. The effect of micas is more uncertain. Existing flow laws for biotite (e.g., Kronenberg et

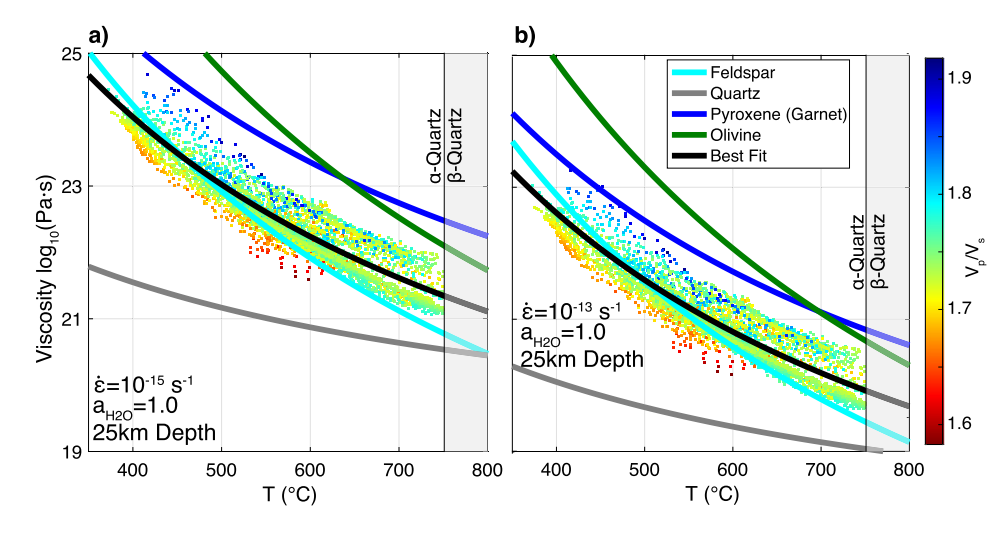


**Fig. 6.** Viscosity at each grid point from Fig. 4a plotted versus temperature calculated at 25 km depth corrected to a  $\dot{\epsilon}$  of  $10^{-15}$  s<sup>-1</sup> (left) or  $10^{-13}$  s<sup>-1</sup> (right) colored by  $V_p/V_s$ . Solid lines represent the predicted viscosities for quartz (grey) (Hirth et al., 2001), plagioclase (light blue) (Rybacki et al., 2006), pyroxene (dark blue) (Dimanov and Dresen, 2005), and olivine (green) (Hirth and Kohlstedt, 2003). Note that garnet is assumed to follow the same flow law as pyroxene (see text for discussion). The black line represents the best-fit flow law to the scattered data (see Eq. (9)).

al., 1990) indicate that biotite is stronger than wet quartz at most lower crustal conditions (T > 400 °C). However, experiments on quartz-muscovite aggregates indicate a factor of 2 weakening with the addition of  $\sim$ 15 vol% mica at 800 °C (Tullis and Wenk, 1994; Tokle et al., 2013). Recalculating equilibrium modes for our total rock database with 0.5 wt% H<sub>2</sub>O, we calculate 0–15 vol% mica in felsic rocks (SiO<sub>2</sub> > 55 wt%) and 0–7 vol% mica in mafic rocks (SiO<sub>2</sub> < 55 wt%). These values imply that the addition of hydrous phases to our relationship between seismic velocities and viscosity would be most significant for felsic rocks. Thus, in regions of low  $V_p/V_s$ , where felsic rocks are predicted to dominate (e.g., Shillington et al. 2015; Jagoutz and Behn, 2013; Hacker et al., 2015), our methodology may systematically overpredict viscosity by up to a factor of two.

At high temperatures and pressures the breakdown of hydrous phases leads to partial melting of the lower crust for certain compositions. These effects are particularly important in compressional regions where the crust is thick (e.g., Tibet) and/or in regimes with high heat flow. Melt decreases viscosity and seismic velocity, especially  $V_s$ , though the exact form of the relationships for crustal rocks remain poorly constrained. For this reason, we have omitted the effect of melt in our predictions. Further, we note that for crustal pressures, melt is typically present only in the  $\beta$ -quartz regime, where we have already shown our inversion poorly constrains viscosity. Thus, if melt is present in regions such as the Salton Trough (Lachenbruch et al., 1985), additional considerations are required to estimate the regional viscosity and stress state. One method to estimate melt is to use magnetotelluric data (Rippe and Unswrorth, 2010). Therefore, it may be possible to invert magnetotelluric and seismic data together to estimate possible rock type and melt fraction in order to bound viscosity.

Another assumption of our methodology is that deformation occurs by wet dislocation creep. For actively deforming regions like Southern California, wet dislocation creep flow laws agree best with viscosities inferred from post seismic creep (e.g., Behr and Hirth, 2014; Freed and Bürgmann, 2004). While diffusion creep is an important mechanism within shear zones, at many lower crustal conditions the equilibrium grain size is typically too large for diffusion creep to be a dominant mechanism (Bürgmann and Dresen, 2008). The impact of shear zones depends on the magnitude of weakening and the volume of the rock the shear zones comprise. For the case of shear zones in mafic rocks, microstructural analyses indicate shear zones decrease the aggregate viscosity by a factor of two to four (Mehl and Hirth, 2008).

Lastly, the Huet et al. (2014) model can only be applied on a scale over which the rock is considered isotropic. In reality, deformation is often localized in shear zones within the lower crust (e.g., Bürgmann and Dresen, 2008; Behr and Platt, 2012) resulting in foliated rocks. Where there is a shear zone fabric, the viscosity is best approximated by the weakest connected phase. The effect of fabric formation is largest at low temperature where the single-phase rheologies differ the most (Fig. 6). Moreover, fabric formation likely affects felsic rocks more than mafic rocks, because felsic rocks weaken to a quartz rheology (e.g., Tullis, 2002), while mafic rocks weaken to a plagioclase rheology (e.g., Mehl and Hirth, 2008). The arrows in Fig. 7c illustrate this effect.

#### 4.2. Seismic-aseismic transition and the brittle-ductile transition

Seismic–aseismic transition, the depth below which few earth-quakes occur, is frequently interpreted as the brittle–ductile transition (e.g., Sibson, 1982). Others interpret seismic–aseismic transition as the depth where friction changes from velocity-weakening to velocity-strengthening (e.g., Scholz, 2002). Here we compare the seismic–aseismic transition in Southern California to the depth of the brittle–ductile transition. We define the locking depth as the depth above which 95% of earthquakes epicenters are located. We use only A and B quality earthquakes from the Southern California Earthquake Data Catalog (http://scedc.caltech.edu/eq-catalogs/) and calculate a locking depth where there are more than 30 magnitude >3.0 earthquakes in a 15 km radius.

The seismic–aseismic transition changes abruptly across the San Andreas Fault (Fig. 7a), with the average locking depth deepening from  $9\pm4$  km to  $15\pm3$  km from east to west. To evaluate the role of temperature and composition on locking depth, we determine the temperature at the locking depth as inferred from the heat flow data. Histograms of temperature at the locking depth exhibit Gaussian distributions with distinct regional means east  $(204\,^{\circ}\text{C})$  and west  $(341\,^{\circ}\text{C})$  of the San Andreas (Fig. 7d). We define the depth to the brittle–ductile transition (Fig. 7b) as the depth where the stress predicted from the aggregate viscosity becomes less than the frictional stress. Frictional stress is calculated assuming a hydrostatic pore-fluid pressure for strike-slip conditions with a friction coefficient of 0.6 (Zoback and Townsend, 2001, Eq. (7b)).

The brittle-ductile transition is systematically deeper than the seismic-aseismic transition across Southern California. In addition, the brittle-ductile transition does not display an abrupt change

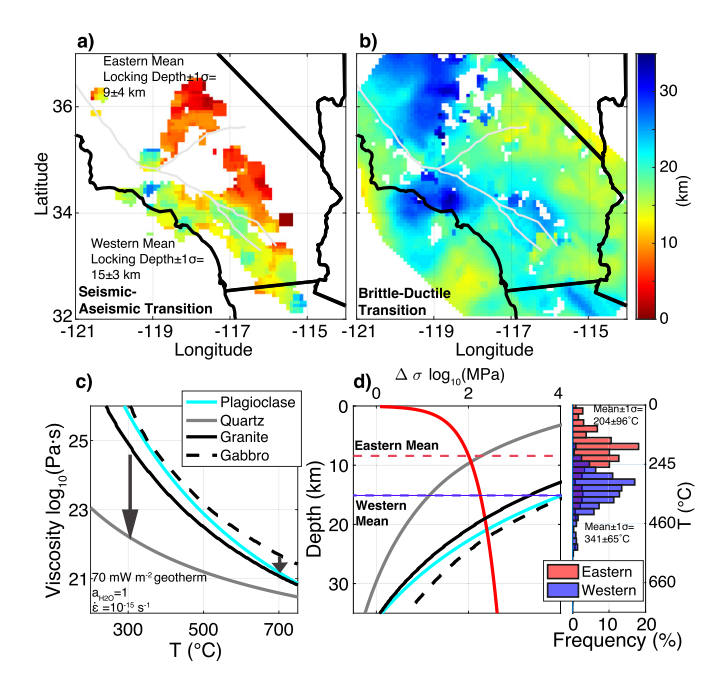


**Fig. 7. a**) Observed regional seismic-aseismic transition. **b**) Predicted brittle-ductile transition, white regions are where the velocity model outputs were continuously anomalous until at least 20 km depth. **c**) Viscosity along a 70 mWm $^{-2}$  ( $\sim 17\,^{\circ}\text{C}\,\text{km}^{-1}$ ) geotherm for quartz and plagioclase wet dislocation creep flow laws as well as calculated aggregate viscosities for a granite and basalt from the rock database. Black arrows show the rheologic effect of fabric formation weakening the granite and gabbro flow laws to their weakest phase, quartz and plagioclase respectively. **d**) Christmas tree stress diagram of a) showing the differential stress as a function of depth for various flow laws and the eastern (solid) and western (dashed) mean locking depths are plotted. Eastern (red) and western (blue) locking depth temperature distributions are shown along the geotherm for reference.

across the San Andreas Fault. The difference between the seismicaseismic transition and the brittle-ductile transition may arise due to fabric formation and/or the presence of hydrous phases. Further, the larger difference between the brittle-ductile transition and the locking depth east of the San Andreas could be linked to compositional variations, where foliated quartz-rich rocks promote more viscous weakening at lower temperatures (Fig. 7c). In fact, the quartzite flow law predicts the eastern locking depths accurately for an average strain rate and geotherm near the San Andreas Fault (Fig. 7d). It is more difficult to constrain what controls the locking depth west of the San Andreas Fault. The locking depth is clearly shallower than the brittle-ductile transition calculated with an aggregate viscosity for either a gabbro or granite. yet significantly deeper than quartz (Fig. 7d). The relatively shallow locking depth could be caused by viscous weakening due to the presence of hydrous phases, a transition to a more lithostatic effective stress (c.f., Hirth and Beeler, 2015), and/or a transition to velocity-strengthening friction.

#### 5. Conclusions

We investigate a new methodology to predict aggregate crustal viscosity given a strain rate, pressure, temperature, and independent estimates of  $V_p$  and  $V_s$ . Our methodology is robust in the  $\alpha$ -quartz regime, but is not robust in the  $\beta$ -quartz regime. Because we do not incorporate hydrous phases, melt, diffusion creep, or strain localization, our aggregate viscosities represent an upper bound, but likely give accurate estimate in regions where strain localization is less important (e.g., higher temperatures).

Applying our methodology to Southern California, we find that viscosity varies by up to four orders of magnitude at 25 km depth, with at least a one and a half order of magnitude variation due to

composition and the remainder due to variations of temperature and strain rate. The aggregate viscosity of the Southern Californian lower crust resembles the wet dislocation creep flow law for plagioclase but is stronger than plagioclase at high temperatures. To address this misfit, we also calculate a best-fit aggregate flow law for Southern California. However, we emphasize that the viscosities calculated using any single flow law would not accurately depict regional variation due to composition. Thus, while temperature is the dominant effect for many actively deforming regions like Southern California, compositional effects are significant and need to be accounted for in geodynamical models of crustal flow. Our method is general, and can easily be applied to other regions; such analyses will be most successful if high quality geophysical data are available to constrain temperature, seismic velocities, and strain rates.

We find that the seismic-aseismic transition deepens abruptly from east to west across the San Andreas Fault. Locking depths east of San Andreas Fault are well fit by the brittle-ductile transition calculated using a quartzite flow law. This observation suggests the importance of fabric formation in shear zones in felsic lithologies immediately beneath the seismogenic zone, in which case the weakest phase (quartz) controls the effective viscosity. The deeper locking depths west of the San Andreas Fault likely reflect changes in composition that inhibit formation of fabrics with a quartz-dominated rheology.

#### Acknowledgements

We would like to thank Wayne Thatcher and David Chapman for their helpful discussions on temperature calculations. We would also like to thank Michael Oskin for an insightful discussion on how to best validate and discuss our methodology. We thank Roland Bürgmann, John Platt, and Editor J.P. Avouac for helpful reviews that improved this manuscript. Funding was provide by NSF Grants EAR-16-24109 (MB), EAR-17-22932 (MB), EAR-16-24178 (GH), EAR-17-22935 (OJ), and SCEC Awards 16106 and 17202 (GH, MB).

#### Appendix A. Supplementary material

Supplementary material related to this article can be found online at https://doi.org/10.1016/j.epsl.2018.04.055.

#### References

Abers, G.A., Hacker, B.R., 2016. A MATLAB toolbox and Excel workbook for calculating the densities, seismic wave speeds, and major element composition of minerals and rocks at pressure and temperature. Geochem. Geophys. Geosyst. 17 (2), 616–624.

Austrheim, H., 1998. The influence of fluid and deformation of metamorphism of the deep crust and consequences for geodynamics of collision zones. In: Hacker, B., Liou, J. (Eds.), When Continents Collide: Geodynamics and Geochemistry of Ultrahigh-Pressure Rocks. Springer, New York, pp. 297–323.

Behr, W.M., Hirth, G., 2014. Rheological properties of the mantle lid beneath the

Behr, W.M., Platt, J.P., 2012. Kinematic and thermal evolution during two-stage exhumation of a Mediterranean subduction complex. Tectonics 31, TC4025. https://doi.org/10.1029/2012TC003121.

Brady, R.J., Ducea, M.N., Kidder, S.B., Saleeby, J.B., 2006. The distribution of radiogenic heat production as a function of depth in the Sierra Nevada Batholith, California. Lithos 86 (3), 229–244.

Bürgmann, R., Dresen, G., 2008. Rheology of the lower crust and upper mantle: evidence from rock mechanics, geodesy, and field observations. Annu. Rev. Earth Planet. Sci. 36, 531–567.

Christensen, N.I., 1996. Poisson's ratio and crustal seismology. J. Geophys. Res. 101 (B2), 3139–3156. https://doi.org/10.1029/95JB03446.

Christensen, N.I., Mooney, W.D., 1995. Seismic velocity structure and composition of the continental crust: a global view. J. Geophys. Res., Solid Earth 100 (B6), 9761–9788.

- Clark, M.K., Bush, J.W., Royden, L.H., 2005. Dynamic topography produced by lower crustal flow against rheological strength heterogeneities bordering the Tibetan Plateau. Geophys. J. Int. 162 (2), 575–590.
- Connolly, J.A.D., 2009. The geodynamic equation of state: what and how. Geochem. Geophys. Geosyst. 10, Q10014. https://doi.org/10.1029/2009GC002540.
- Cottrell, E., Kelley, K.A., 2011. The oxidation state of Fe in MORB glasses and the oxygen fugacity of the upper mantle. Earth Planet. Sci. Lett. 305, 270–282.
- Dimanov, A., Dresen, G., 2005. Rheology of synthetic anorthite-diopside aggregates: implications for ductile shear zones. J. Geophys. Res., Solid Earth 1978 (2012). 110(B7).
- Ducea, M., Saleeby, J., 1998. A case for delamination of the deep batholithic crust beneath the Sierra Nevada, California. Int. Geol. Rev. 40 (1), 78–93.
- Durham, W.B., Mirkovich, V.V., Heard, H.C., 1987. Thermal diffusivity of igneous rocks at elevated pressure and temperature. J. Geophys. Res., Solid Earth 92 (B11) 11615-11634
- England, P.C., Walker, R.T., Fu, B., Floyd, M.A., 2013. A bound on the viscosity of the Tibetan crust from the horizontality of palaeolake shorelines. Earth Planet. Sci. Lett. 375, 44–56.
- Freed, A.M., Bürgmann, R., 2004. Evidence of power-law flow in the Mojave desert mantle. Nature 430 (6999), 548–551.
- Freed, A.M., Bürgmann, R., Herring, T., 2007. Far-reaching transient motions after Mojave earthquakes require broad mantle flow beneath a strong crust. Geophys. Res. Lett. 34 (19).
- Hacker, B., 2008. H<sub>2</sub>O subduction beyond arcs. Geochem. Geophys. Geosyst. 9 (3), Q03001. https://doi.org/10.1029/2007GC001707.
- Hacker, B.R., Christie, J.M., 1990. Brittle/ductile and plastic/cataclastic transitions in experimentally deformed and metamorphosed amphibolite. In: Duba, A.G., et al. (Eds.), The Brittle–Ductile Transition in Rocks. In: Geophys. Monogr. Ser., vol. 56. AGU, Washington, DC, pp. 127–147.
- Hacker, B.R., Kelemen, P.B., Behn, M.D., 2015. Continental lower crust. Annu. Rev. Earth Planet. Sci. 43, 167–205.
- Hanchar, J.M., Miller, C.F., Wooden, J.L., Bennett, V.C., Staude, J.M.G., 1994. Evidence from xenoliths for a dynamic lower crust, eastern Mojave desert, California. J. Petrol. 35 (5), 1377–1415.
- Hirth, G., Beeler, N.M., 2015. The role of fluid pressure on frictional behavior at the base of the seismogenic zone. Geology 43 (3), 223–226.
- Hirth, G., Kohlstedt, D., 2003. Rheology of the upper mantle and the mantle wedge: a view from the experimentalists. In: Inside the Subduction Factory, pp. 83–105.
- Hirth, G., Teyssier, C., Dunlap, J.W., 2001. An evaluation of quartzite flow laws based on comparisons between experimentally and naturally deformed rocks. Int. J. Earth Sci. 90 (1), 77–87.
- Huang, Y., Chubakov, V., Mantovani, F., Rudnic, R.L., McDonough, W.F., 2013. A reference Earth model for the heat-producing elements and associated geoneutrino flux. Geochem. Geophys. Geosyst. 14 (6), 2003–2029.
- Huet, B., Yamato, P., Grasemann, B., 2014. The Minimized Power Geometric model: an analytical mixing model for calculating polyphase rock viscosities consistent with experimental data. J. Geophys. Res., Solid Earth 119 (4), 3897–3924.
- Humphreys, E.D., Coblentz, D.D., 2007. North American dynamics and western US tectonics. Rev. Geophys. 45 (3).
- Jagoutz, O., Behn, M.D., 2013. Foundering of lower island-arc crust as an explanation for the origin of the continental Moho. Nature 504 (7478), 131–134.
- Jagoutz, O., Schmidt, M.W., 2012. The formation and bulk composition of modern juvenile continental crust: the Kohistan arc. Chem. Geol. 298, 79–96.
- Ji, S., Martignole, J., 1994. Ductility of garnet as an indicator of extremely high tem-
- perature deformation. J. Struct. Geol. 16 (7), 985–996. Jull, M., McKenzie, D., 1996. The effect of deglaciation on mantle melting beneath
- Iceland. J. Geophys. Res., Solid Earth 101 (B10), 21815–21828. Karato, S.I., 2012. Deformation of Earth Materials: An Introduction to the Rheology
- of Solid Earth. Cambridge University Press.

  Karato, S.I., Wang, Z., Liu, B., Fujino, K., 1995. Plastic deformation of garnets: systematics and implications for the rheology of the mantle transition zone. Earth
- Planet. Sci. Lett. 130 (1–4), 13–30. Kelemen, P.B., Behn, M.D., 2016. Formation of lower continental crust by relamination of buoyant arc lavas and plutons. Nat. Geosci. 9, 197–205.
- Kelemen, P.B., Hanghøj, K., Greene, A.R., 2014. One view of the geochemistry of subduction-related magmatic arcs, with an emphasis on primitive andesite

- and lower crust. In: Rudnick, R.L. (Ed.), Treatise on Geochemistry, 2nd, vol. 4. Elsevier–Pergamom, pp. 746–805.
- Kelley, K.A., Cottrell, E., 2012. The influence of magmatic differentiation on the oxidation state of Fe in a basaltic arc magma. Earth Planet. Sci. Lett. 329, 109–121.
- Kraner, M., Holt, W.E., Borsa, A.A., 2018. Seasonal non-tectonic loading inferred from cGPS as a potential trigger for the M6.0 South Napa Earthquake. J. Geophys. Res., Solid Earth. https://doi.org/10.1029/2017/B015420.
- Kronenberg, A.K., Kirby, S.H., Pinkston, J., 1990. Basal slip and mechanical anisotropy of biotite. J. Geophys. Res. 95 (B12), 19,257–19,278. https://doi.org/10.1029/JB095iB12p19257.
- Lachenbruch, A.H., Sass, J.H., Galanis, S.P., 1985. Heat flow in southernmost California and the origin of the Salton Trough. J. Geophys. Res., Solid Earth 90 (B8), 6709–6736.
- Lee, E.J., Chen, P., Jordan, T.H., Maechling, P.B., Denolle, M.A., Beroza, G.C., 2014. Full 3-D tomography for crustal structure in southern California based on the scattering-integral and the adjoint-wavefield methods. J. Geophys. Res., Solid Earth 119 (8), 6421–6451.
- Lowry, A.R., Pérez-Gussinyé, M., 2011. The role of crustal quartz in controlling Cordilleran deformation. Nature 471 (7338), 353–357.
- Mehl, L., Hirth, G., 2008. Plagioclase preferred orientation in layered mylonites: evaluation of flow laws for the lower crust. J. Geophys. Res., Solid Earth 113 (B5).
- Pollack, H.N., Chapman, D.S., 1977. On the regional variation of heat flow, geotherms, and lithospheric thickness. Tectonophysics 38 (3–4), 279–296.
- Rippe, D., Unsworth, M., 2010. Quantifying crustal flow in Tibet with magnetotelluric data. Phys. Earth Planet. Inter. 179 (3-4), 107-121.
- Rudnick, R.L., Fountain, D.M., 1995. Nature and composition of the continental crust: a lower crustal perspective. Rev. Geophys. 33 (3), 267–309.
- Rybacki, E., Gottschalk, M., Wirth, R., Dresen, G., 2006. Influence of water fugacity and activation volume on the flow properties of fine-grained anorthite aggregates. J. Geophys. Res., Solid Earth (1978–2012) 11 (B3).
- Scholz, C.H., 2002. The Mechanics of Earthquakes and Faulting. Cambridge University
- Shi, X., Kirby, E., Furlong, K.P., Meng, K., Robinson, R., Wang, E., 2015. Crustal strength in central Tibet determined from Holocene shoreline deflection around Siling Co. Earth Planet. Sci. Lett. 423, 145–154.
- Shillington, D.J., Van Avendonk, H.J., Behn, M.D., Kelemen, P.B., Jagoutz, O., 2013. Constraints on the composition of the Aleutian arc lower crust from VP/VS. Geophys. Res. Lett. 40 (11), 2579–2584.
- Shinevar, W.J., Behn, M.D., Hirth, G., 2015. Compositional dependence of lower crustal viscosity. Geophys. Res. Lett. 42 (20), 8333–8340.
- Sibson, R.H., 1982. Fault zone models, heat flow, and the depth distribution of earthquakes in the continental crust of the United States. Bull. Seismol. Soc. Am. 72 (1), 151–163.
- Thatcher, W., Pollitz, F.F., 2008. Temporal evolution of continental lithospheric strength in actively deforming regions. GSA Today 18 (4/5), 4.
- Tokle, L., Stunitz, H., Hirth, G., 2013. The effect of muscovite on the fabric evolution of quartz under general shear, Abstract T53A-2559 presented at 2013 Fall Meeting. AGU. San Francisco. Calif.. Dec.
- Tullis, J., 2002. Deformation of granitic rocks: experimental studies and natural examples. Rev. Mineral. Geochem. 51 (1), 51–95.
- Tullis, J., Wenk, H.R., 1994. Effect of muscovite on the strength and lattice preferred orientations of experimentally deformed quartz aggregates. Mater. Sci. Eng. A 175 (1), 209–220.
- Williams, C.F., DeAngelo, J., 2011. Evaluation of approaches and associated uncertainties in the estimation of temperatures in the upper crust of the Western United States. Trans., Geotherm. Resour. Counc. 35, 1599–1605.
- Xu, L., Mei, S., Dixon, N., Jin, Z., Suzuki, A.M., Kohlstedt, D.L., 2013. Effect of water on rheological properties of garnet at high temperatures and pressures. Earth Planet. Sci. Lett. 379, 158–165.
- Zandt, G., Gilbert, H., Owens, T.J., Ducea, M., Saleeby, J., Jones, C.H., 2004. Active foundering of a continental arc root beneath the southern Sierra Nevada in California. Nature 431 (7004), 41–46.
- Zoback, M.D., Townend, J., 2001. Implications of hydrostatic pore pressures and high crustal strength for the deformation of intraplate lithosphere. Tectonophysics 336 (1), 19–30.